# A Functional Form for the Diurnal Variation of Lake Surface Temperature on Lake Hartwell, Northwestern South Carolina

J. L. Hodges, J. R. Saylor, and N. B. Kaye

***Abstract*—Satellite measurements of water surface temperature can benefit several environmental applications such as predictions of lake evaporation, meteorological forecasts, and predictions of lake overturning events, among others. Limitations on the temporal resolution of satellite measurements can restrict these improvements. A model of the diurnal variation in lake surface temperature could potentially increase the effective temporal resolution of satellite measurements of surface temperature, thereby enhancing the utility of these measurements in the above applications. As a step in this direction, herein a one-dimensional thermal model of a lake is used in combination with surface temperature measurements from the moderate resolution imaging spectroradiometer instrument aboard the Aqua and Terra satellites, along with ambient atmospheric conditions from local weather stations, to calculate the diurnal surface temperature variation for Lake Hartwell in South Carolina. The calculated solutions are used to obtain a functional form for the diurnal surface temperature variation of this lake, a result which has not been obtained heretofore. This functional form was obtained by averaging over several years worth of data and, therefore, represents the diurnal variation of surface temperature of the average day. Accordingly, attempts to use this averaged function to predict surface temperature in between satellite overpasses on any given day did not perform well due to day-to-day variations in cloud cover, wind speed, and other factors. It is possible that use of this averaged function combined with daily meteorological data may enable better performance.**

***Index Terms*—Infrared imaging, lakes, remote sensing, surface temperature measurement.**

## I. Introduction

THE air/water interface of lakes and reservoirs is the location where numerous environmentally relevant transport processes are mediated. These include the transfer of dissolved gases such as oxygen and carbon dioxide, the transfer of heat to and from the atmosphere, and the evaporation and condensation of water at the surface. All of these processes depend critically on the water surface temperature $T_s$, which affects or controls the driving force for all of the transport processes listed above. In addition, predictions of lake overturning, precipitation, and the global climate all depend to varying degrees on $T_s$.

Until the 1980s when sea surface temperature measurements via satellite became available, it was difficult to obtain measurements of $T_s$ over the surface of a body of water having any significant horizontal extent [1]. Even low-cost thermistors or thermocouples require some form of buoy system with a power supply and data acquisition capability, all of which makes it a challenge to deploy enough sensors to ascertain the spatial variation of $T_s$. Moreover, waves can cause the sensor to move below or above the water surface, introducing significant uncertainties in measurements of $T_s$ obtained in this way. Recent advancements in satellite remote sensing allow for measurements of $T_s$ over large areas and with reasonable spatial resolution. When dealing with satellite measurements, there is always some tradeoff between spatial and temporal resolution. For example, USGS LANDSAT images of the visible and infrared spectrum are obtained with a spatial resolution of 30 m, but with a temporal resolution of approximately once every 16 days [2]. This spatial resolution is excellent; however, if knowledge of diurnal variation is desired, the temporal resolution is insufficient. Similarly, the advanced very high resolution radiometer (AVHRR) aboard the MetOp satellite has excellent temperature resolution but has a revisit time of approximately once every five days [3]. The moderate resolution imaging spectroradiometer (MODIS) satellites on the other hand have a spatial resolution of 1000 m obtained twice daily. The two MODIS satellites, Aqua and Terra, follow a similar orbit but have a temporal offset of approximately 3 h. By compiling data from these two satellites a maximum of four measurements per day can be obtained [4]. Of course in locations where there is cloud cover for a significant portion of the year, no amount of satellite measurements will enable sufficient measurements of the water surface temperature, and other methods must be pursued.

While a temporal resolution of four satellite measurements per day may be satisfactory in some cases, for many applications this resolution will be inadequate since it will be difficult obtaining even a daily maximum and minimum $T_s$, for example. Having a functional form for the diurnal variation in $T_s$ could potentially enable development of methods to increase the temporal resolution of satellite-obtained measurements of $T_s$. While several studies exist where MODIS data were used to study and/or model the surface temperature of lakes, [5]–[15] a functional form for the diurnal variation in surface temperature was not developed in any of these studies. There exists a study in the area of bulk-to-skin temperature difference where

Manuscript received December 3, 2015; revised March 29, 2016; accepted April 14, 2016. Date of publication May 17, 2016; date of current version August 24, 2016. This work was supported by the USGS through the South Carolina Water Resources Center. Access to temperature measurements of Lake Hartwell was provided by the U.S. Army Corps of Engineers. *(Corresponding author: John R. Saylor)*

J. L. Hodges is with the Department of Mechanical Engineering, Virginia Tech, Blacksburg, VA 24061 USA (e-mail: johodges@vt.edu).

J. R. Saylor is with the Department of Mechanical Engineering, Clemson University, Clemson, SC 29634-0921 USA (e-mail: jsaylor@clemson.edu).

N. B. Kaye is with the Department of Civil Engineering, Clemson University, Clemson, SC 29634 USA (e-mail: nbkaye@clemson.edu).

Digital Object Identifier 10.1109/JSTARS.2016.2555798

the diurnal variation was observed. This was done by Wilson *et al*. [16] and is similar to the classical studies on the thin skin effect in air/sea interfacial research, such as the work of Grassl [17], McAlister and McLeish [18], and Katsaros *et al*. [19]. However, in this study, a function for the diurnal variation in $T_s$ also was not developed. Such a function would be of some fundamental importance in limnology. Also, knowledge of the surface temperature can be used to estimate evaporation. This can be done by using $T_s$ to obtain the surface water vapor concentration and, combined with a mass transfer method and local NWS measurements of air temperature, wind speed, and relative humidity, obtain the evaporative flux from a lake surface [20]. Though not the focus of this study, such an approach could enable developments in global water cycle prediction using remotely sensed $T_s$ by increasing the ability to estimate evaporation from many of the world's lakes.

Herein, a one-dimensional (1-D) model of a lake is used in combination with $T_s$ measurements from Aqua and Terra, and measurements of air temperature $T_a$, wind speed $u$, and relative humidity $\phi$, from the NWS automated surface observing system (ASOS) [21] to calculate the diurnal surface temperature variation. Using the data obtained from the simulations presented herein, the general functional form for the diurnal variation in $T_s$ is developed. Simulations were conducted for Lake Hartwell located in northwestern South Carolina. Lake Hartwell has an average depth of 14 m, a maximum depth of 56 m, and a surface area of 230 km$^2$, and is located at an elevation of 201 m above mean sea level. Hartwell is a reservoir that was completed in 1962 and is operated by the United States Army Corps of Engineers (USACE). It is part of the Savannah River Basin (SRB) and is one of the five major lakes in the upper Savannah River, the other four being Lakes Jocassee, Keowee, Russell, and Thurmond. The SRB serves as a water resource for a population in Georgia, South Carolina, and North Carolina that exceeds 1.5 million (USACE, 2013). Hartwell in particular is becoming stressed as a consequence of population and economic growth, and better models for predicting water levels in this lake will be needed to manage growing demand. Evaporative loss is a poorly predicted portion of the water balance and knowledge of daily, as well as seasonal variations in the surface water temperature is critical to improving predictions of evaporative loss and the lake water level in general. This serves as another long-term motivation for this study.

Given that the model developed herein is 1-D, its applicability is limited to situations where spatial variations in $T_s$ are limited. As such, direct application of this study to the global water cycle is left as future work where more sophisticated (three-dimensional) model development may reveal spatial variation in the diurnal cycle. Nevertheless, this study may have significant application to smaller scale situations such as smaller scale lakes and how the diurnal variation in $T_s$ affects biological processes, heat loads, and water balances in such lakes.

## II. Methods

The 1-D model of the lake used here was developed by applying conservation of energy at the water surface, and within the mixed layer, and applying a turbulent kinetic energy balance within the mixed layer. These equations were solved to obtain $T_s$ in the time intervals between the Aqua and Terra measurements of $T_s$. Satellite measurements of $T_s$ were only obtained using MODIS pixels that were completely free of land (including islands). Pixels were chosen based on visual examination of GIS data of Lake Hartwell obtained from USACE resulting in a total of 12 pixels. The LST MODIS data product was used herein which uses the MOD11A1 and MYD11A1 LST products generated from MODIS bands 31 (11 $\mu$m) and 32 (12 $\mu$m) using a split-window algorithm designed for a variety of surfaces, including land and inland water surfaces [22]. The LST products are already processed to account for surface emissivity and atmospheric attenuation. The LST data also includes a cloud mask that is only set to one when the confidence of clear-sky conditions is 66% or larger [11], [22]. Pixels where the mask was set to zero were not used.

The energy balance equations are now presented.

### A. *Conservation of Energy at the Surface*

The surface energy balance is calculated following the method presented by Alcântara *et al*. [23]. The primary energy fluxes which contribute to the net heat flux at the surface $\Phi_N$ are the incident shortwave radiation $\Phi_s$, the long wave radiation $\Phi_{\mathrm{ri}}$, the sensible heat flux $\Phi_{\mathrm{sf}}$, and the latent heat flux $\Phi_{\mathrm{evap}}$ [23], [24]. Thus, neglecting the effects of precipitation, chemical and biological reactions, and kinetic energy (e.g., from wind, waves, etc.), the net energy flux at the lake surface is [24] and [23]:

$$\Phi_N = \Phi_s(1 - A) - (\Phi_{\mathrm{ri}} + \Phi_{\mathrm{sf}} + \Phi_{\mathrm{evap}}) \tag{1}$$

where $A$ is the albedo of water, and $\Phi_{\mathrm{evap}}$ is the energy flux due to evaporation or condensation. When $\Phi_N$ is positive, there is a net flux of energy into the lake.

The incident shortwave radiation is

$$\Phi_s = b_1 \Phi_0 (\sin d)^{b_2} (1 - 0.65C^2) \tag{2}$$

where the two calibration parameters $b_1$ and $b_2$ are determined from radiometer data to be 0.79 and 1.15, respectively, [23], $\Phi_0$ is the solar constant, 1390 W/m$^2$, $d$ is the solar elevation angle, and $C$ is the cloud cover index which varies between zero and unity and was obtained from MODIS L2 data [4], [23], [24]. The solar elevation angle was calculated using the method presented by Reda and Andreas [25]. The net longwave radiation flux is

$$\Phi_{\mathrm{ri}} = \epsilon\sigma T_s^4(0.39 - 0.05e_a^{1/2})(1 - \lambda C) + 4\epsilon\sigma T_s^3(T_s - T_a) \tag{3}$$

which is positive when there is a loss of energy from the lake, and where $\epsilon = 0.97$ is the thermal infrared emissivity of water [23], $\sigma$ is the Stefan–Boltzmann constant, $\lambda$ is the Reed correction factor [23], [26], [27], and $e_a$ is the partial pressure of water vapor,

$$e_a = \phi e_{\mathrm{sat}}(T_a) \tag{4}$$

where $e_{\mathrm{sat}}$ is the saturated vapor pressure in mb using the equation due to Lowe [28]

$$\begin{aligned} e_{\mathrm{sat}}(T) = \; & 6984.505294 - 188.9039310 \times T + 2.133357675 \times T^2 \\ & - 1.288580973 \times 10^{-2} \times T^3 \\ & + 4.393587233 \times 10^{-5} \times T^4 - 8.023923082 \times 10^{-8} \\ & \times T^5 + 6.136820929 \times 10^{-11} \times T^6 \end{aligned} \tag{5}$$

where $T$ is temperature in $K$. This equation is valid only over liquid water and not ice. The sensible heat flux is calculated using the equation

$$\Phi_{\text{sf}} = \rho_a c_{p_a} c_H u_{10}(T_s - T_a) \quad (6)$$

where $\rho_a$ is the air density, $c_{p_a}$ is the specific heat capacity of air, $u_{10}$ is the wind velocity 10 m above the water surface, and $c_H$ is a coefficient of turbulent exchange [23], [29]. The energy flux due to evaporation is

$$\Phi_{\text{evap}} = \rho_a c_E h_{\text{fg}} u_{10}(e_{\text{sat}}(T_s) - \phi e_{\text{sat}}(T_a)) \frac{0.622}{P_a} \quad (7)$$

where $h_{\text{fg}}$ is the latent heat of vaporization for water, $P_a$ is the atmospheric air pressure, and $c_E$ is another coefficient of turbulent exchange [23], [29].

The following assumptions are made in the development of (1)–(7). First, the electromagnetic spectrum is lumped into two separate bands (shortwave and long wave radiation), which assumes a step change in the spectral response of water, as is commonly done in limnology [23]. Next, the latent and sensible heat fluxes are assumed to be functions of ($T_s, T_a, u_{10}, \phi$), with the remaining complexity being summed up in the turbulent exchange coefficients, $C_H$ and $C_E$ [(6) and (7)]. Finally, the short wave radiation is only included during the day, its effects being negligible at night [23]; the other terms in (1) are included at all times in the day and night.

### B. Conservation of Energy of the Mixed Layer

Most lakes exhibit some degree of thermal stratification, and the temperature distribution in a stratified lake is typically described by three distinct layers: the mixed layer (epilimnion), the metalimnion (thermocline), and the hypolimnion where lateral temperature variations are ignored. The mixed layer is the region closest to the surface in which buoyant forces and/or convective forces mix the layer, yielding a layer of finite thickness where the temperature is essentially uniform. Hence, in the simulations presented here, the temperature of the mixed layer and the surface temperature are made equal and are both referred to as $T_s$. The metalimnion is the region of sharp temperature change in the lake. The hypolimnion is the quiescent region of the lake which changes temperature slowly from season to season. The temperature of this layer is referred to as the bulk lake temperature, $T_b$.

Lake Hartwell is a monomictic lake, having a single mixing season which lasts through the winter [30]. As shown in Fig. 1, a 1-D mixed layer model is used to simulate this lake where the lake is divided into two uniform temperature regions: the mixed layer at temperature $T_s$ and the hypolimnion at a temperature $T_b$. Data on the change in temperature with depth in the thermocline is often used in lake models to increase the simulation accuracy. However, such data were not available and so the thermocline is modeled as a step change in temperature. With this assumption in mind, $L$ from the simulation should be thought of as an effective mixed layer depth for the whole lake rather than a precise measure of mixed layer depth. The control volume used for this model is shown in Fig. 1. The general equation for

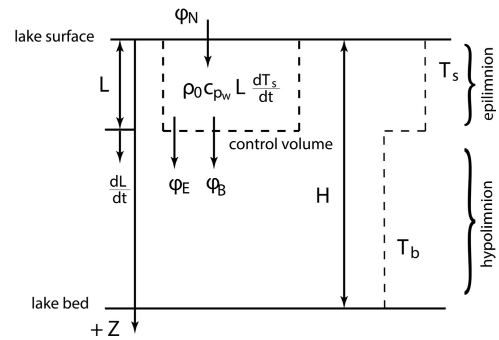


Fig. 1. Control volume of the mixed layer where $L$ is the mixed layer depth, $H$ is the lake depth, $\rho_0$ is the reference water density, $c_{p_w}$ is the specific heat capacity of water, $T_s$ is the mixed layer temperature, $T_b$ is the bulk lake temperature, $\Phi_N$ is the net surface flux, and $\Phi_E$ is energy flux due to entrainment.

conservation of energy of the control volume is

$$\rho_0 c_{p_w} L \frac{dT_s}{dt} = \Phi_N - \Phi_E - \Phi_B \quad (8)$$

where $\rho_0$ is the reference water density, $c_{p_w}$ is the specific heat capacity of water, $L$ is the mixed layer depth and the energy flux due to entrainment, $\Phi_E$ is calculated using

$$\Phi_E = \rho_0 c_{p_w} (T_s - T_b) \frac{dL}{dt}. \quad (9)$$

The energy flux due to the heat transfer to the hypolimnion, $\Phi_B$ is calculated using

$$\Phi_B = \rho_0 c_{p_w} (H - L) \frac{dT_b}{dt} \quad (10)$$

where $H$ is the lake depth. It is noted that $\Phi_E$ is the energy required to change the temperature of the entrained fluid to match $T_s$, and $\Phi_B$ is the energy required to change $T_b$.

Combining (8), (9), and (10) and rearranging terms yields an equation for the time rate of change of $T_s$:

$$\frac{dT_s}{dt} = \frac{\Phi_N}{c_p \rho_0 L} - \frac{(T_s - T_b)}{L} \frac{dL}{dt} - \frac{(H - L)}{L} \frac{dT_b}{dt}. \quad (11)$$

### C. Turbulent Kinetic Energy Budget

Since (1) and (11) have three unknowns ($\frac{dT_s}{dt}$, $L$, and $\frac{dL}{dt}$) these two equations are not a closed system. To close the system, the turbulent kinetic energy budget is used. The mixed layer depth, $L$, increases due to wind and buoyant mixing, and these effects are modeled in the turbulent kinetic energy budget as a change in potential and kinetic energy of the entrained water from the hypolimnion. As water is entrained, the control volume increases in size, changing the center of gravity of the control volume, and the velocity of the entrained fluid is accelerated to the turbulent state of the mixed layer [31].

The turbulent kinetic energy budget is calculated following the method presented by Fischer *et al*. [31]. The equation for the time rate of change of the mixed layer depth is

$$\frac{dL}{dt} = \frac{C_k^f q_*^3}{C_T q_*^2 + \alpha (T_s - T_b) g L} \quad (12)$$

where $C_k^f$ is the internal losses coefficient, $\alpha$ is the volumetric thermal expansion coefficient of water, $g$ is the acceleration due to gravity, $C_T$ is the kinetic energy coefficient, and $q_*$ is the combined velocity scale [31]

$$q_*^3 = (w_*^3 + \eta^3 u_*^3) \tag{13}$$

where $\eta$ is the net efficiency of introduction of kinetic energy at the surface, $u_*$ is the shear velocity, modeled as

$$u_* = \sqrt{\frac{\rho_a C_D u_{10}^2}{\rho_0}}. \tag{14}$$

$C_D$ is the drag coefficient, modeled as [23]

$$C_D = 0.00052 u_{10}^{0.44} \tag{15}$$

and $w_*$ is the buoyant velocity scale [31], [32]

$$w_* = \left(\frac{\alpha g \Phi_N L}{C_{p_w} \rho_0}\right)^{1/3}. \tag{16}$$

The constants $C_T$ and $\eta$ were set to 0.5 and 1.75, respectively, as recommended by Fischer *et al*. [31]. There are, of course, many assumptions inherent in the use of (12), including the assumption of a 1-D mixed layer; that internal losses are proportional to buoyancy input; that energy input to the layer from wind and from penetrative convection are cumulative, as well as others. The interested reader is directed to Fischer *et al*. [31].

Preliminary simulations showed that the solution was most sensitive to the value of the internal loses coefficient, $C_k^f$, which determines how quickly the mixed layer responds to a change in ambient parameters. The default value of $C_k^f = 10$ was used in the simulation; however in certain instances the simulations are iterated over $C_k^f$ to decrease the errors in the simulations (simulation error is defined below). The method for choosing when to iterate over $C_k^f$ versus using a constant value is described in Section II-E.

### D. Winter Algorithm

Lake Hartwell is a warm climate monomictic lake experiencing overturn and complete mixing during the winter [33]. This corresponds to the seasonal mixed layer depth extending to the lake bottom, which the simulations presented herein predict. Since the lake is no longer stratified under such conditions, the assumptions used in the model described above are invalid. Specifically, during overturn $T_s$ would remain essentially constant for the entire season since there is not enough energy on a diurnal time scale to significantly change the temperature of the entire bulk of the lake in a single day. However from satellite measurements it is known that $T_s$ varies significantly during the course of a day in the winter and that $T_s$ deviates from bulk temperature measurements. Hence, a different simulation algorithm was needed for the winter.

Other 1-D models were examined such as a conduction in stagnant water approach [34], [35]. However these methods assume that the mixing effects of wind are negligible, which is not the case for Lake Hartwell in the winter. The eddy coefficient hypothesis presented by Niiler and Kraus [36] was considered; however, this method depends greatly on empirically determined coefficients which would likely not be constant for the duration of the simulation. The mixed layer model presented by Spigel [37] was considered; however, it required more knowledge of the development of the diurnal thermocline than was available for this study, e.g., thermocline thickness, inclination, and the existence of many thermoclines from previous history. Momentum balance methods such as that proposed by Imberger [32] were considered as well; however, poor agreement was found between simulation results and the satellite measurements during overturn.

Here, the same method described in Section II-A–II-C was used but with a constant effective mixed layer depth for the winter. When the simulation predicts overturn, $L$ is set to a constant value which minimizes the residual error between simulation results and satellite measurements. Herein, a default value of 1.1 m was used for this constant; however, similar to $C_k^f$ mentioned in the previous section, $L$ was varied between satellite measurements to reduce error. This approach will be described more fully in Section II-E. The winter start and end dates, chosen so as to minimize the simulation error at satellite measurements, were November 15 and March 31, respectively, though the simulations were not overly sensitive to these dates.

### E. Simulation Algorithm

Simulations were conducted from the summer of 2002 which is the earliest time at which two daily satellite measurements were available from both Aqua and Terra, and run through the beginning of the summer of 2014. An assumed value for $L$ based on the seasonal thermocline was used as an initial condition. The inputs consist of four daily $T_s$ measurements from Aqua and Terra, hourly ambient atmospheric conditions from the Anderson airport weather station (KAND) in Anderson, SC, USA ($T_a$ and $\phi$), and measurements of $T_b$ obtained from USACE. Ideally the ambient parameters would be measured on the lake; however, historical measurements were not available over the desired time interval. Multiple weather stations were considered for obtaining ($T_a$ and $\phi$), and the Anderson airport was used since it is the weather station closest to the center of Lake Hartwell. A concatenation of third-order polynomial curve fits (one for each year) was developed for $T_b$ based on the 6 to 12 $T_b$ measurements which were available from USACE each year. Note that year refers to calendar year herein. The polynomial fit to the data was obtained via a least squares fit to the data. The measurements were obtained using a Hydrolab MS5 variable resistance thermistor and were obtained primarily at the dam. The $T_b$ values used herein were the maximum depth values of the temperature profiles obtained by USACE. To ensure the polynomial fits were continuous, the initial point of each year was forced to match the final point of the polynomial curve for the previous year. For five years (2004, 2006, 2007, 2013, and 2014), the temporal resolution of the measurements was insufficient to create a good fit. For these years, the average yearly trend from all of the other years in the simulation time period were used to create a fit for $T_b$, with a vertical offset based on the final temperature from the previous year. The developed

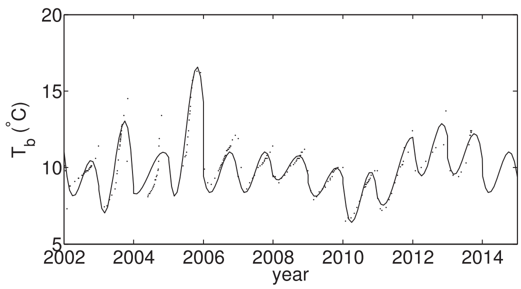


Fig. 2. Lake Hartwell bulk temperature measurements, $T_b$ versus time. The data from USACE is denoted by the points, and the solid line is the polynomial curve fit created from the data.

curve fit was used herein for the simulation. The resulting concatenated curve fit for $T_b$ is presented in Fig. 2 along with the USACE data used in developing it. This fit was used to obtain values for $T_b$ in the simulations.

Using $u_{10}$ from KAND yielded poor agreement with satellite measurements of $T_s$. Accordingly, the simulations were iterated over $u_{10}$ to minimize the rms deviation of $T_s$ from satellite measurements. It has been shown that $u_{10}$ can vary significantly both temporally and spatially over bodies of water compared to land measurements [38]. The consequences of this approach are presented in Section V.

The details of the solution algorithm are presented below and are illustrated using a flow chart in Fig. 3. An example of the converged simulation for $T_s$ between two satellite points is presented in Fig. 4. In the following description, $t$ corresponds to the time since the first satellite measurement, $t^1_{\rm sat}$, and is incremented in time steps of $\Delta t = 60$ s.

For each pair of satellite measurements, the following process was performed. First, the net flux at the surface was calculated using (1)–(7). Next, $\frac{dL}{dt}$ was calculated using (12)–(16). Then, $\frac{dT_s}{dt}$ was calculated using (11). New values for $T_s$ and $L$ were then obtained using the equations:

$$T_s(t+\Delta t) = T_s(t) + \frac{dT_s}{dt}\Delta t \tag{17}$$

and

$$L(t+\Delta t) = L(t) + \frac{dL}{dt}\Delta t. \tag{18}$$

The above process was repeated until $t$ was equal to the time of the next satellite measurement, $t^{n+1}_{\rm sat}$. As noted above, this process was repeated over a range of $u_{10}$ to give a solution with the least deviation of the simulation from the satellite measurements. The approach for doing this was to first run a simulation for $u_{10}$ equal to 0 and 20 m/s. An example of this is shown in Fig. 5. As this figure shows, both values of $u_{10}$ yield values of $T_s$ at $t^{n+1}_{\rm sat}$ unequal to the satellite measurement; however, the satellite measurement is between the two solutions. Thus, the next step was a straightforward iteration over $u_{10}$ to find the converged solution, i.e., the solution where $T_s$ at the second satellite measurement time was as close as possible to that second satellite measurement. An example of such a converged solution is shown in Fig. 4. The procedure for iterating over $u_{10}$

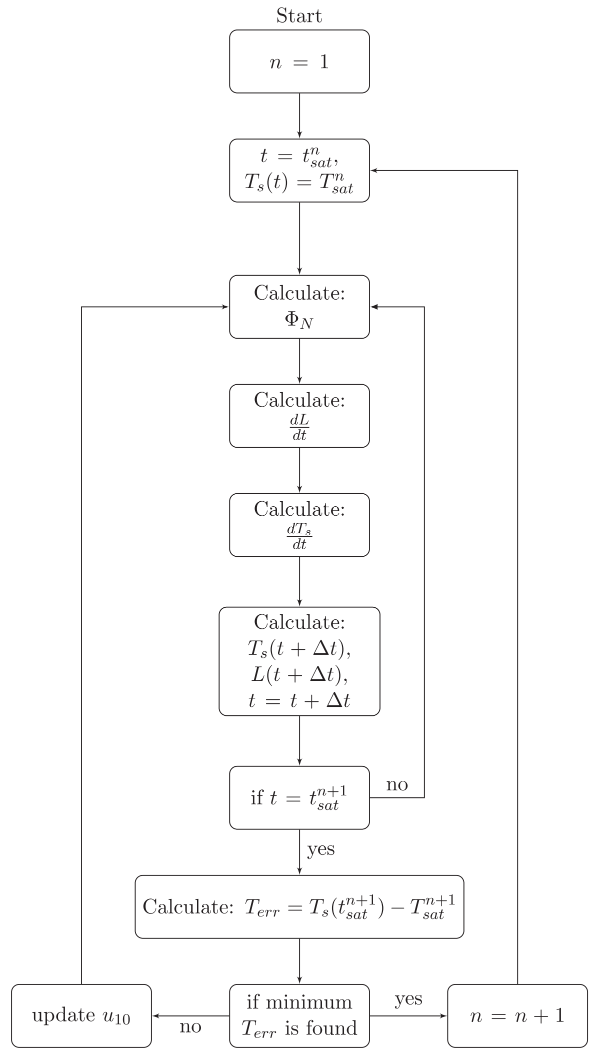


Fig. 3. Simulation algorithm flow chart. Process starts with the first pair of satellite measurements and continues until the 12 year simulation time period is complete.

began by first computing the error for a given pair of satellite points which was defined as

$$T_{\rm err} = \left|T_s(t^{n+1}_{\rm sat}) - T^{n+1}_{\rm sat}\right| \tag{19}$$

where $T_s(t^{n+1}_{\rm sat})$ is the simulated temperature, and $T^{n+1}_{\rm sat}$ is the satellite-measured temperature. The next value of $u_{10}$ was calculated using linear interpolation from the previous $u_{10}$ and the $u_{10}$ at which $T_{\rm err}$ was minimum. The process was repeated until $u_{10}$ converged to within 0.001 m/s. Typical values of $T_{\rm err}$ ranged from 0 to 2 K.

In certain cases, the two initial values for $u_{10}$ used ($u_{10} = 0$ m/s and $u_{10} = 20$ m/s) gave two values of $T_s$ at $t^{n+1}_{\rm sat}$ that did not span the value of $T^{n+1}_{\rm sat}$. An example of such a situation is shown in Fig. 6 where both of the simulations give values of $T_s$ at $t^{n+1}_{\rm sat}$ that are less than the satellite measurement. Since $T_s$ is typically monotonic in $u_{10}$ (when all other parameters are held constant) a second parameter must be varied in these cases to adjust the range of possible solutions until the satellite measurement falls between the two simulated values (this assumes that for Lake

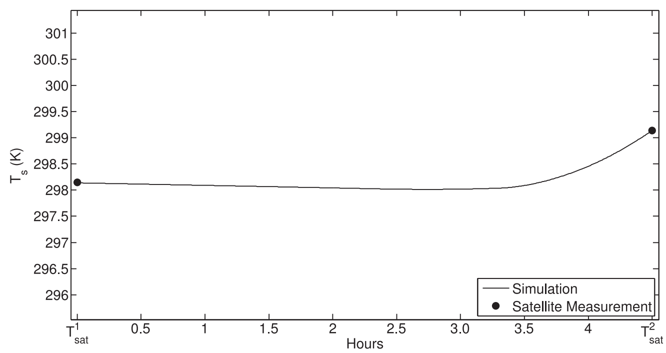


Fig. 4. Example of converged simulated $T_s$ versus time in hours between two satellite measurements.

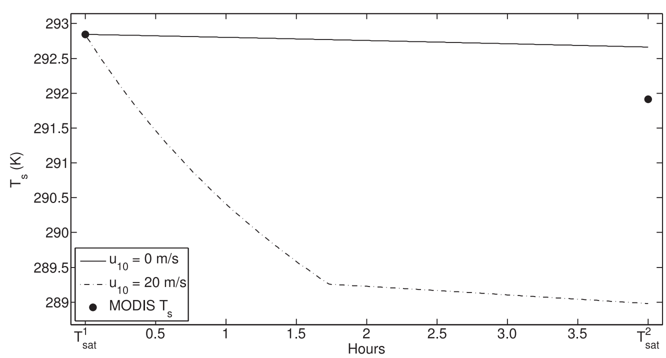


Fig. 5. Simulation for $T_s$ using $u_{10} = 0$ m/s and $u_{10} = 20$ m/s. Note that one simulation gives a final value of $T_s$ greater than $T_{\mathrm{sat}}^2$ and the other gives a final value of $T_s$ less than $T_{\mathrm{sat}}^2$. This enables a straightforward iteration over $u_{10}$ to find the converged solution.

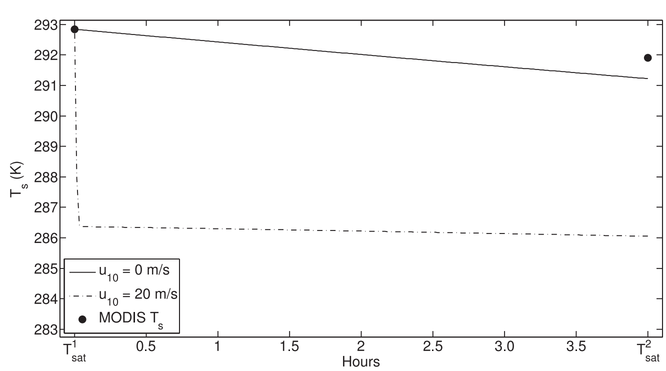


Fig. 6. Simulation for $T_s$ using $u_{10} = 0$ m/s and $u_{10} = 20$ m/s. Note that both simulations give values of $T_s$ less than $T_{\mathrm{sat}}^2$. Thus $T_{\mathrm{sat}}^2$ does not reside in the range of possible solutions for these two wind speeds.

Hartwell, $0\,\mathrm{m/s} < u_{10} < 20$ m/s, which is a safe assumption). The result of this is shown in Fig. 7 where $C_k^f$ was varied to force upward the two $T_s$ solutions shown in Fig. 6, thereby spanning the satellite measurement. In the spring, summer, and fall, $C_k^f$ was used as the second parameter, forcing upward (or downward) the solutions for the initial guesses of $u_{10} = 0$, 20 m/s if necessary. However, as noted in Section II-D, varying $C_k^f$ in the winter does not significantly affect the solution and

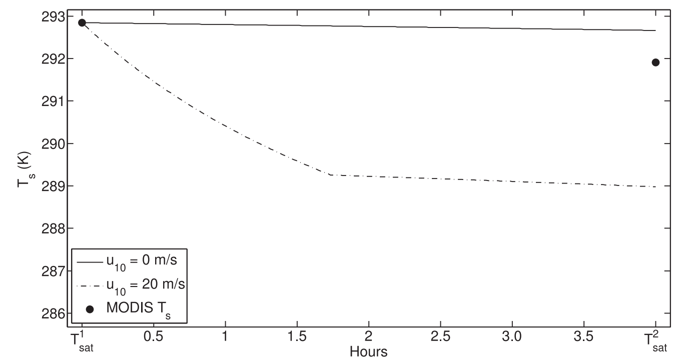


Fig. 7. Simulation for $T_s$ using $u_{10} = 0$ m/s and $u_{10} = 20$ m/s after iterating over $C_k^f$. Note that one simulation gives $T_s > T_{\mathrm{sat}}^2$ and the other gives $T_s < T_{\mathrm{sat}}^2$. This enables a straightforward iteration over $u_{10}$ to find the converged solution.

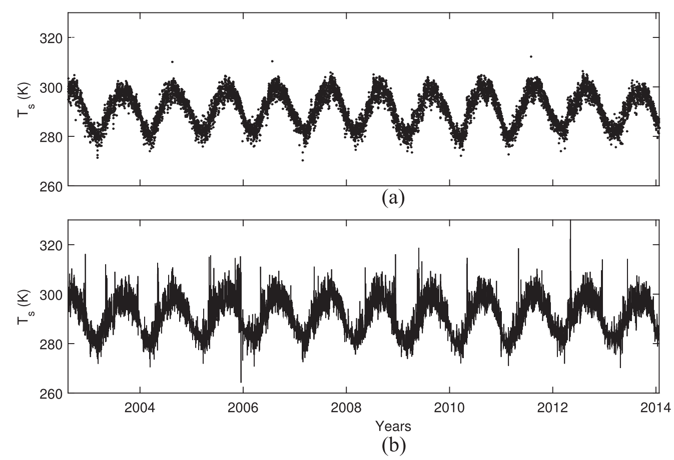


Fig. 8. Surface temperature, $T_s$, in K versus date in years: (a) Satellite measurements only, (b) simulation results.

so $L$ was used as the second parameter that was varied in the winter simulations, when necessary.

Once the satellite value for $T_s$ fell within the possible solutions for $T_s$, $u_{10}$ was varied to force the $T_s$ solution to hit the satellite point as discussed earlier. The solution with the minimum residual error calculated using (19) was selected and the simulation then proceeded to the next satellite point and set of ambient parameters.

## III. Results

Fig. 8(a) presents the satellite measurements of $T_s$ for the entire 12 year period of record considered, and Fig. 8(b) presents the simulations for $T_s$. Due to the density of the data, individual satellite measurements and simulation points are difficult to see in Fig. 8 and shorter time durations are plotted below. Fig. 8(b) shows some instances where the simulations deviate significantly from any of the measured values as well as from any of the other simulated values. The cause of this is described in Section V. Less than 0.1% of the $T_s$ points are larger (smaller) than the maximum (minimum) $T_{\mathrm{sat}}$.

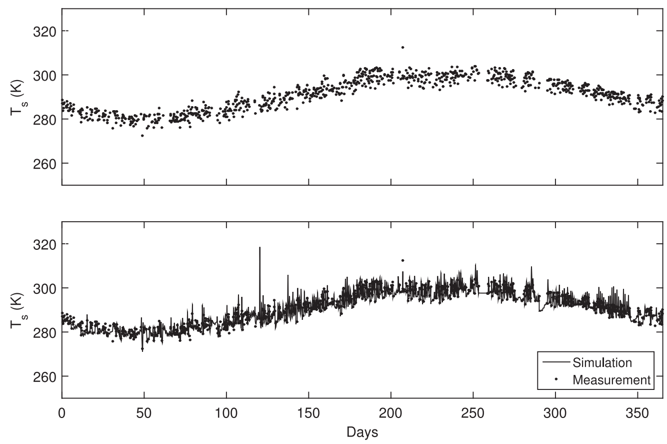


Fig. 9. Surface temperature, $T_s$, in K versus day number for 2011. Day 0 corresponds to January 1, 2011: (a) Satellite measurements only (dots), (b) satellite measurements and simulation results (line).

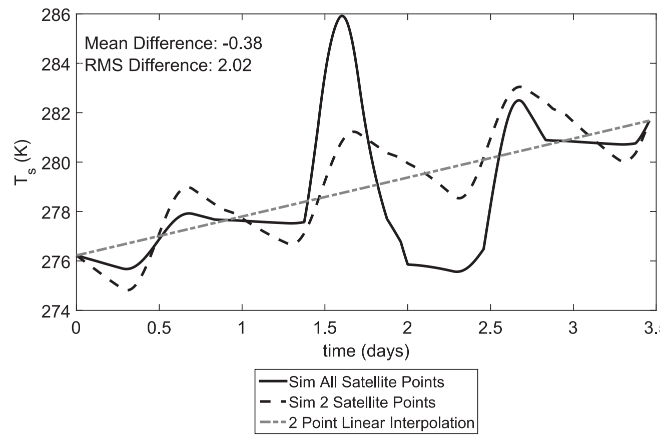


Fig. 10. Plot of simulated $T_s$ versus time in days. The solid black line includes all satellite measurements in the time period, while the dashed line employs only the satellite data at day 0 and day 3.5. The average and rms difference between the solid black and dashed line are indicated in the inset. The straight gray line is the value of $T_s$ obtained via a simple linear interpolation.

A measure of the validity of the simulations is the degree to which integrating (17) forward from one satellite point resulted in hitting the next satellite point. The rms deviation of the model result from the satellite point $T'$ was used as a figure of merit of the model validity:

$$T' = \left[\frac{1}{N}\sum_{n=1}^{N}\left(T_{\mathrm{err}}^{n}\right)^2\right]^{1/2} \tag{20}$$

where $T_{\mathrm{err}}$ is defined in (19) and $N$ is the total number of satellite measurements. Using the entire dataset (save for four out of a total of 10 402 satellite points where the simulation diverged), gave a value of $T' = 1.4$ K. However, as noted above and shown in Fig. 8(b), occasionally there were spurious points which contributed disproportionately to $T'$. To eliminate the effect of these points in computing $T'$, the rms of $T_{\mathrm{sat}}$, $\sigma_{\mathrm{sat}}$ was computed and all simulation points that fell outside of $\pm\sigma_{\mathrm{sat}}$ of the mean simulation temperature were ignored in computing $T'$, giving $T' = 0.83$ K. The ignored data represented 4.58% of the total simulated $T_s$. As will be shown in Section V, this compares well with the uncertainty in MODIS measurements in general. Another measure of the validity of the simulations is Willmotts index of agreement [39] for the difference between the model and the data. For the entire period of record explored here this index was 0.949, where unity signifies perfect agreement.

The seasonal variation in $T_s$ can be seen in Fig. 8 and is shown more clearly in Fig. 9 where simulations from a sample year (2011) are presented. Starting on January 1, 2011 (Day 0 in Fig. 9), $T_s$ drops until it reaches a minimum around the middle of February, then steadily increases until it reaches a maximum in the middle of August, and finally begins to decrease until the end of the year.

Obviously the simulations depend critically on satellite measurements of $T_s$. Cloud cover often precludes such measurements, sometimes for more than one day at a time. To determine the effect of $T_s$ data loss of, say, three days in a row, simulations were conducted for a portion of the period of record where data was purposely ignored for three days, and compared with those obtained using the data. An example of this is shown in Fig. 10, showing the importance of the satellite data in the model.

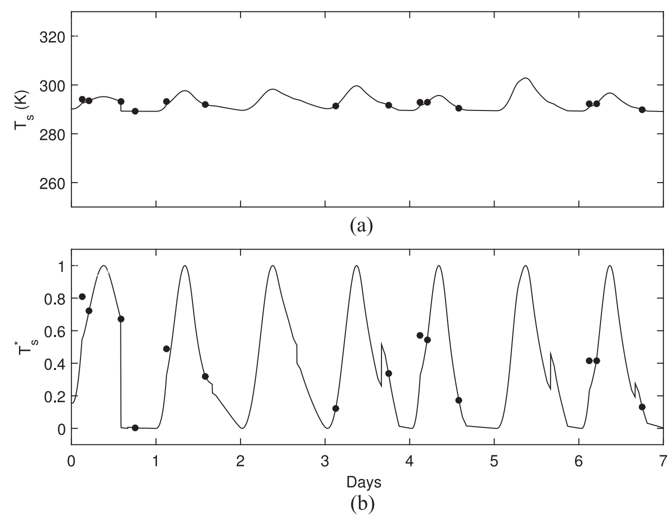


Fig. 11. For both plots the simulation results (solid line) and satellite measurements (filled circles) are both presented. (a) $T_s$ in K versus time in days for a sample week. (b) $T_s^*$, from (21) of the sample week in part (a).

To focus on the diurnal variation, the simulations for a sample week are shown in Fig. 11(a) which shows that the largest $T_s$ is generally found in the early afternoon, and the coolest slightly before sunrise. To obtain the diurnal variation in the surface temperature using the entire dataset, a nondimensional temperature $T^*$ is developed so as to prevent seasonal trends from obscuring the diurnal trend:

$$T^* = \frac{T - T_{\min}}{T_{\max} - T_{\min}}. \tag{21}$$

Here, the subscripts $\min$ and $\max$ correspond to the minimum and maximum values of each individual day. A time trace of $T_s^*$ for a sample week is presented in Fig. 11(b). To further prevent obscuration of the diurnal trend by the seasonal trend, a nondimensional time scale $t^*$, was used to define time based on

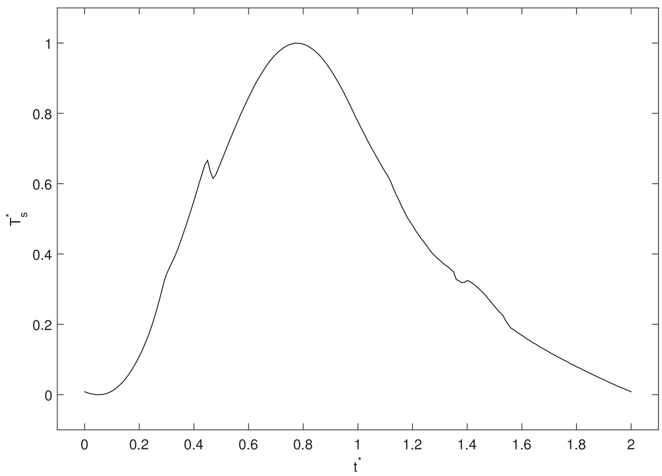


Fig. 12. Average plot of $T_s^*$ versus $t^*$ for the entire simulation period (2002–2014).

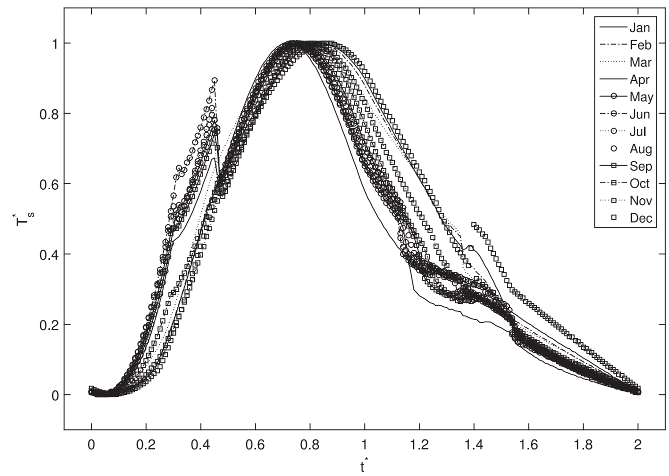


Fig. 13. Average plot of $T_s^*$ versus $t^*$ for each month for the entire simulation period (2002–2014).

local sunrise and sunset time

$$t^* = \begin{cases} \dfrac{24 + t - t_{\text{set}}}{24 - t_{\text{set}} + t_{\text{rise}}} + 1 & 0 \le t < t_{\text{rise}} \\ \dfrac{t - t_{\text{rise}}}{t_{\text{set}} - t_{\text{rise}}} & t_{\text{rise}} \le t < t_{\text{set}} \\ \dfrac{t - t_{\text{set}}}{24 - t_{\text{set}} + t_{\text{rise}}} + 1 & t_{\text{set}} \le t < 24 \end{cases}. \quad (22)$$

In (22), $t_{\text{rise}}$ and $t_{\text{set}}$ are sunrise and sunset in hours since midnight local time. Hence, $t^* = 0$ at sunrise on the current day, $t^* = 1$ at sunset, and $t^* = 2$, its maximum value, at sunrise the following day. This scaling has a few key advantages over using local time. The growth of a new thermocline begins at sunrise when the surface layer begins to absorb solar energy. Using this scaling ensures that this growth begins at the same $t^*$ every day, which is useful for averaging purposes across multiple days. Additionally, since solar position and length of day are key parameters in modeling the diurnal variation of $T_s$, averaging the results from different parts of the year using $t$ instead of $t^*$ may conceal diurnal trends that are common for the whole year, a further advantage of using $t^*$.

A plot of $T_s^*$ versus $t^*$ obtained using all days of the 12 year simulation period is presented in Fig. 12. This is the trend averaged over all months and for all years of the period of record. Each month gave a different plot, though the overall trend was the same. This is shown in Fig. 13 where the average over the period of record for each month is presented. The standard deviation about the mean for each $t^*$ in Fig. 13 was computed, and in Fig. 14 the average trend was replotting along with the trends one standard deviation above and below the average, showing the degree of variation about the mean for each $t^*$ due to monthly variation.

The goal of this study is to develop a functional description of the diurnal variation of lake surface temperature. Moreover, the desire is to develop a function with four fitting parameters so that the known surface temperatures obtained from the four daily measurements which can be obtained from Aqua and Terra, potentially, can be used to develop an individual equation for

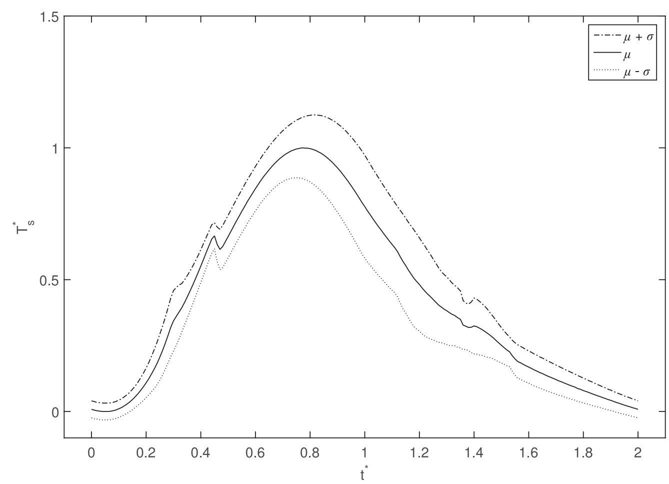


Fig. 14. Average plot of $T_s^*$ versus $t^*$ for the entire simulation period (2002–2014), with a plot which is one standard deviation greater than and less than the average. The standard deviation was obtained from the monthly plots presented in Fig. 13. The average plot in this figure is the same as that presented in Fig. 12.

any given day. To do this, the Fourier transform was taken of the data presented in Fig. 12, and the first four components of that transform were used to create a functional form for the diurnal variation in $T_s^*$. The FFT is presented in Fig. 15 showing the primary harmonic at 0.5, which is expected since $t^*$ has a fixed period of 2, along with the higher harmonics, including the second, third, and fourth harmonics at $f^* = 1, 1.5$, and 2, where $f^*$ is the dimensionless frequency. Accordingly, using four Fourier components, $T_s^*$ may be represented as

$$T_s^*(t^*) = \sum_{k=1}^{4} \left[ B_k \sin\left(2\pi f_k^* t^* - \psi_k\right) \right] - D \quad (23)$$

where $k$ is the harmonic, $f_k^*$ is the dimensionless frequency of the harmonic, $B_k$ is the amplitude of each Fourier component, $\psi_k$ is the phase shift for each Fourier component, and $D$ is a dc offset. The goal was to use the four daily satellite measurements from Aqua and Terra to obtain four unknowns in an equation like

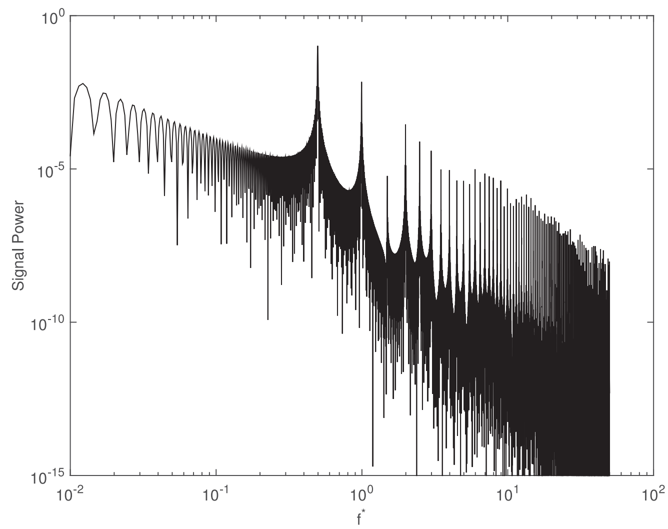


Fig. 15. Fourier transform of data presented in Fig. 12.

TABLE I
VALUES FOR CONSTANTS IN (23)

| $k$ | $B_k$ | $f_k$ | $\psi_k$ |
|---|---|---|---|
| 1 | 0.4547 | 0.5 | 1.03 |
| 2 | 0.1182 | 1.0 | 2.81 |
| 3 | 0.0041 | 1.5 | 6.85 |
| 4 | 0.0241 | 2.0 | 9.40 |
| $D = -0.4354$ | | | |

(23) for any given day. Of course (23) actually has nine unknown constants, not four. However, by iterative solution, all of $B_k, \psi_k$, and $D$ can be obtained to match any four satellite measurements. Iterative solution was also used to obtain the optimal values of $(B_k, \psi_k, D)$ for the $(t^*, T_s^*)$ data presented in Fig. 12, the plot of $T_s^*$ versus $t^*$, averaged over every day of the 12 year simulation period. These values are summarized in Table I. For this averaged plot, the peak temperature occurs at $t^* = 0.77$, and the minimum temperature occurs at $t^* = 0.05$. Thus, the peak occurs a few hours before sunset and the minimum shortly after sunrise. This reconstruction is shown along with the original average $(t^*, T_s^*)$ results in Fig. 16.

## IV. DATA AND MODEL VALIDATION

The results presented above depend on the accuracy of the MODIS data which were used as an input to the model. Ground truth sensors for $T_s$ were not available on Lake Hartwell for the period of record investigated. Accordingly, to ascertain the effect of errors and uncertainty in the MODIS data on the results, we resorted to the literature. Specifically, we used the validation study presented in Crosman and Horel [11] where MODIS measurements were compared to thermocouple measurements obtained at a depth of 0.5 m, and a bias and rms deviation of the satellite measurements from ground truth were obtained. This study is similar to our study in that it used the LST MODIS product and provides a detailed analysis of MODIS water surface temperature uncertainty.

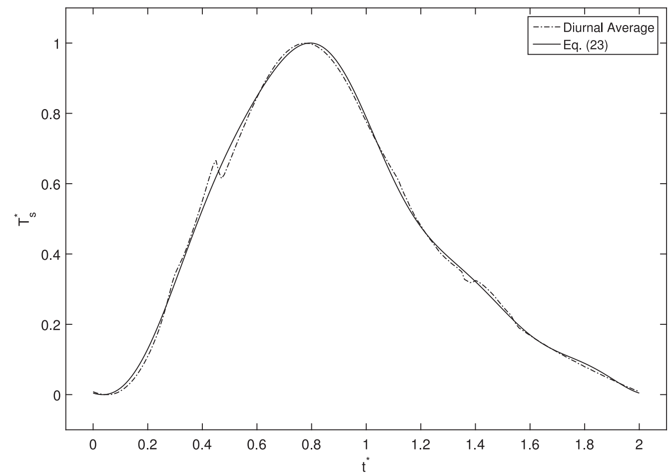


Fig. 16. Average $T_s^*$ versus $t^*$ obtained from the simulation results for 2002–2014 compared with (23).

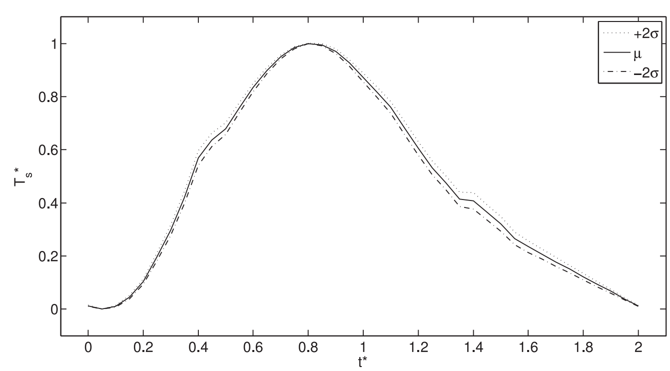


Fig. 17. Plot of $T_s^*$ versus t* obtained by perturbing the satellite measurements by a random value having an rms of 1.6 K and a mean of zero. The average of 500 simulations is plotted as $\mu$. At each point in time, a point located two rms $(2\sigma)$ above and below $(-2\sigma)$ the average plot is included, showing the impact of the uncertainty in the input satellite data on the model output.

Crosman and Horel [11] report an rms of the deviation of the MODIS measurement from the ground truth value of 1.6 K. To assess the effect of a variability of this magnitude on our results, we reran the simulations, adding a random value to each satellite measurement. The random value was presumed Gaussian with an rms of 1.6 K and a mean of zero (the effect of bias is addressed below). This was repeated 500 times, giving 500 time traces like that shown in Fig. 12. These 500 time traces were used to compute an average and an rms at each point in time. These results are plotted in Fig. 17 for the dimensionless form and in Fig. 18 for the dimensional form. In each figure, the average time trace is presented along with a point located at twice the rms above and twice the rms below the average at each point in time. Due to computational restrictions, only one year of data were used to obtain Figs. 17 and 18. Fig. 17 shows that the uncertainty in the satellite measurements of $T_s$ result in a $\pm 2$ rms uncertainty in $T_s^*$ that is less than 0.1 for virtually all $t^*$. Fig. 18 shows that this variability is less than 0.5 K for

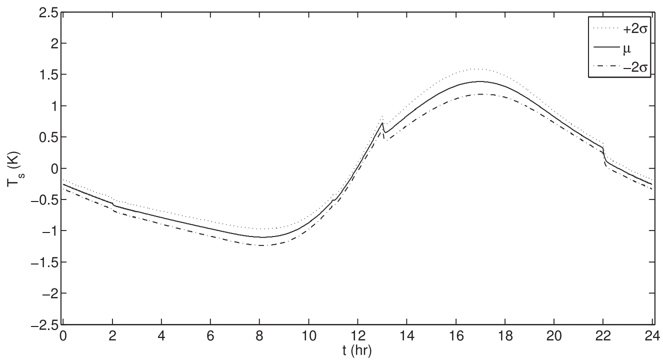


Fig. 18. Plot of $T_s$ versus $t$ obtained in the same way as described in Fig. 17, but in dimensional terms.

TABLE II
VALUES FOR CONSTANTS IN (23), OBTAINED FOR THE CASE WHERE THE SATELLITE DATA POINTS WERE PERTURBED BY A 1.6 K RANDOM VALUE

| $k$ | $B_k$ | $f_k$ | $\psi_k$ |
|---|---|---|---|
| 1 | 0.4641 | 0.5 | 1.17 |
| 2 | 0.0975 | 1.0 | 2.71 |
| 3 | 0.0232 | 1.5 | 2.32 |
| 4 | 0.0186 | 2.0 | 9.76 |
| $D = -0.4876$ | | | |

These constants are for the $+2\sigma$ plot shown in Fig. 17.

TABLE III
VALUES FOR CONSTANTS IN (23), OBTAINED FOR THE CASE WHERE THE SATELLITE DATA POINTS WERE PERTURBED BY A 1.6 K RANDOM VALUE

| $k$ | $B_k$ | $f_k$ | $\psi_k$ |
|---|---|---|---|
| 1 | 0.4619 | 0.5 | 1.15 |
| 2 | 0.1053 | 1.0 | 2.94 |
| 3 | 0.0139 | 1.5 | 2.22 |
| 4 | 0.0185 | 2.0 | 9.66 |
| $D = -0.4583$ | | | |

These constants are for the $-2\sigma$ plot shown in Fig. 17.

virtually all $t$. Moreover, in both of these plots, it is clear that the qualitative trend of the functional form is not affected by a 1.6 K uncertainty in the satellite data.

To see the magnitude of the effect of this uncertainty on the functional form of $T_s^*$, the values of $B_k$, $\psi_k$, and $D$ were recalculated for the $+2\sigma$ version and the $-2\sigma$ version of the function shown in Fig. 17, and are presented in Table II and III, respectively. These tables show small changes for the constants when $k = 1$, as expected.

To ascertain the effect of a bias error in the MODIS data on the simulations, a constant value was subtracted from each satellite measurement of $T_s$ and the simulations were then conducted as described in Section II. The results of this are presented in Figs. 19 and 20 for the dimensional and dimensionless cases, respectively, where the results of the simulations are presented for a range of biases from $-2.5$ to 2.5 K in increments of 0.5 K. Fig. 19 shows that a positive bias results in increased maximum to minimum variation in the diurnal cycle when plotted in dimensional coordinates. This is not seen in Fig. 20, the dimensionless $T_s^*$ versus $t^*$ plot, as is expected from the form of the nondimensionalization [(21)]. For both plots, the qualitative form of the diurnal variation is not changed by the bias error in the satellite measurement. The bias cited by Crosman and Horel [11] was $-1.5$ K when the satellite measurements were compared to their *in situ* measurements, which is one of the biases plotted in Figs. 19 and 20.

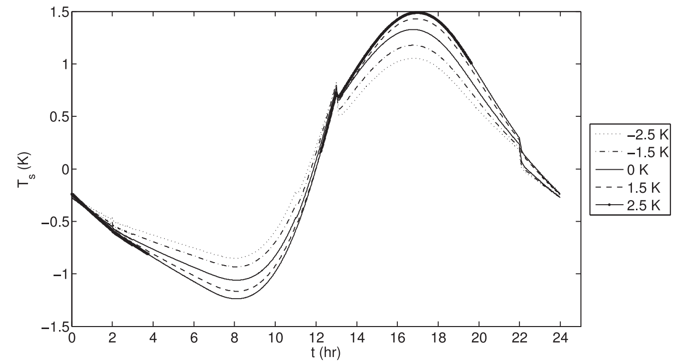


Fig. 19. Plot of $T_s$ versus $t$ obtained by first biasing the satellite data by the value indicated in the legend.

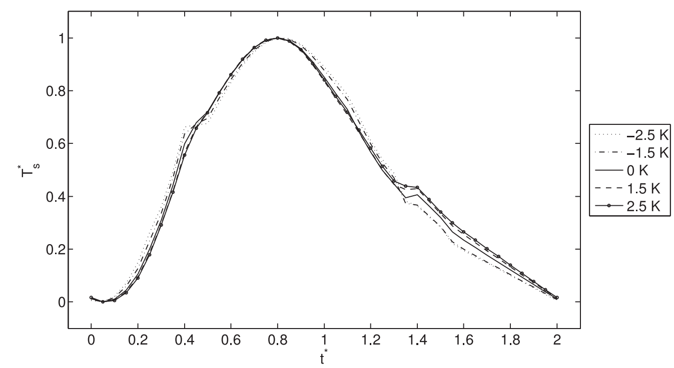


Fig. 20. Plot of $T_s^*$ versus $t^*$ obtained by first biasing the satellite data by the value indicated in the legend. Note that the ordinate is non-dimensional.

Of course, there is no reason to believe that the rms and bias errors presented in Crosman and Horel [11] are exactly the same as those which would be the case for Lake Hartwell. However, a review of MODIS data validation on inland lakes reveals rms deviations between MODIS measurements and *in situ* measurements that are comparable, or smaller than that observed by those researchers. For example, MODIS measurements obtained by Grim *et al*. [7] over the Great Salt Lake, yielded a MODIS-to-buoy measurement bias of 0.01 K and a mean average error of 0.66 K (after bias adjusting). Liu *et al*. [5] validated MODIS LST products over Lake Taihu, China, and found an rms error between the MODIS data and *in situ* measurements ranging from 1.2 to 1.8 K. Oesch *et al*. [13] investigated MODIS data compared to *in situ* measurements on Lake Constance. These results varied for Aqua and Terra and for day and night conditions. The average bias was $-0.23$ K and the average rms deviation of MODIS measurements from *in situ* measurements was 1.25 K. For Lakes Vättern and Vänern in Sweden, Reinart and Reinhold [12] observed a mean absolute difference of 0.41 K between the MODIS measurement and *in situ* measurements obtained from thermometers located at a depth of 0.5 m, and a standard deviation of 0.40 K. Finally, in a study of Qinghai Lake, a terminal lake in China, an rms deviation was observed between the MODIS surface water temperature and *in situ* measurements from a sensor located 0.5 m beneath the water surface of 1.46 K [9]. Even for situations where land (not water) surface temperatures are measured, the rms deviations observed by Crosman and Horel [11] are comparable or larger than those of other studies. For example, Coll *et al*. [40] found bias errors of $-0.3$ K and a rms deviation of 0.6 K over homogeneous rice fields. Summarizing, the rms deviation of 1.6 K observed by Crosman and Horel [11] is comparable to or larger than the studies cited above, with the only exception being the high end of the range of rms deviations observed by Liu *et al*. [5]. Even for the case of a different satellite platform, Landsat, only a mean square error of 0.53 K was found for Landsat imagery over Lake Constance [41]. Hence, our perturbations used to assess the effect of uncertainty in the MODIS data that we presented in Figs. 17 and 18, can be viewed as representing an upper bound in deviation of the satellite measurements from the actual surface temperature. Finally, we note that the approach that we take here, where we use uncertainty measurements from a lake different from that under study, is not dissimilar from that taken by Schneider and Hook [42], for example, who obtained water surface temperatures on 167 inland water bodies using AVHRR data, and used ground truth obtained on the Great Lakes, but not for the other inland water bodies which they studied.

We also computed statistics of the MODIS values and the simulation values at the satellite overpass times. The goal was to determine if a statistic of higher order than the mean showed similarity between the simulation and the measurement. The rms of the MODIS measurements at the 0200, 1100, 1300, and 2200 overpass times were 6.7 K, 6.6 K, 6.6 K, and 6.5 K, respectively, while the corresponding values for the simulations were 6.2 K, 6.3 K, 6.7 K, and 6.9 K. This gives an average difference of the rms of the simulations from MODIS of 4.9%. The skewness was also computed, however, there were not sufficient data to result in converged statistics of this higher order moment.

## V. Discussion

To our knowledge, (23) is the first functional description of the diurnal variation in $T_s$ for a lake. This complicates comparison with the literature. We note that a similar approach was taken by Strong *et al*. [6] who used a slab model approach to study the surface temperature of the Great Salt Lake. In that work, the mixed layer depth (effective lake depth) was also treated as a variable and was adjusted to improve model performance. That work was more detailed and sophisticated than that presented here in that a model of the atmosphere was coupled to their lake model. However, results on diurnal variations were not reported.

Jin and Dickinson [43] obtained a diurnal variation for the land surface skin temperature diurnal cycle (LSTD). This function is presented in Fig. 21, along with that obtained here showing the similarities and differences between the two models. Similar to what is presented here, the LSTD model uses a min/maxed temperature in terms of local sunrise and sunset times. The LSTD authors propose a sinusoidal fit between sunrise and sunset, however, for the period from sunset to midnight they use a power law fit, and a linear fit from midnight to sunrise. For lake surface temperature, the minimum occurs at approximately the same time as for LSTD; however, the peak time is later in the day on the lake than on land. Both of these observations are expected due to the larger thermal inertia of a lake compared with that of land whose surface temperature would be expected to respond more rapidly to radiative forcing.

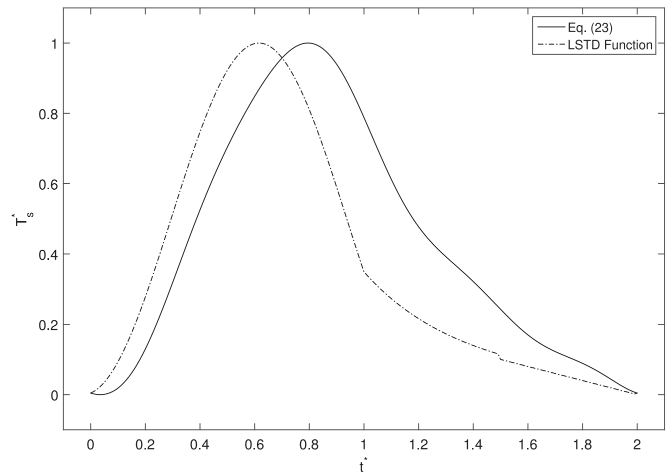


Fig. 21. Plot of $T_s^*$, versus $t^*$ for the results developed herein and that of the LSTD model due to Jin and Dickinson [43].

A possible use of the diurnal function presented in (23) could be to obtain $T_s$ at times in between satellite overpasses for any given day. This is unlikely to perform with great accuracy since (23) was obtained by averaging over daily data for several years; it is simply the form of the average day. Hour-to-hour variations in cloud cover, wind speed, as well as precipitation will cause significant deviations of $T_s$ for any given day from (23). Hence, the development of (23) should be seen as just a step in the direction of improving the effective temporal resolution of MODIS measurements of lake surface temperature. Nevertheless, an attempt is made here to use (23) to obtain $T_s$ in between satellite overpasses.

Figs. 22 and 23 present $T^*$ versus $t^*$ for two sample days. Here, the four daily satellite measurements were fit to (23). Fitting was accomplished by generating a linear set of four equations and then solving for $B_1$ through $B_4$ in (23) for the day. The values for $f_k$, $\psi_k$, and $D$ were obtained from Table I, i.e., the values obtained when fitting to the entire data simulation period. The figures show that (23) agrees reasonably well with the satellite data. The agreement is not as good in between the satellite points, as expected. An alternative approach is to use the four average MODIS measurements for each individual month at each satellite overpass time (thus four points per month). In this method, $T^*_{\mathrm{sat}}$ at each overpass time was assumed equal to $T^*$ of the ideal trend shown in Fig. 16 at the equivalent $t^*$. What

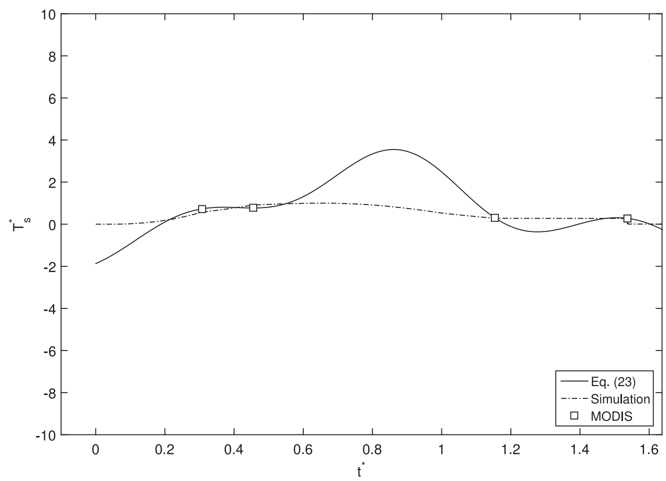


Fig. 22. Plot of $T_s^*$ versus $t^*$ for the satellite data, the simulations, and (23) for a sample day.

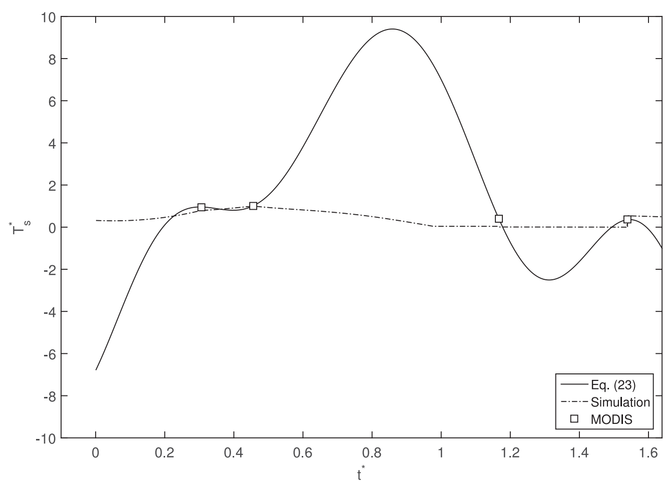


Fig. 23. Plot of $T_s^*$ versus $t^*$ for the satellite data, the simulations, and (23) for a sample day.

is needed then is a value for $T_{\max}$ and $T_{\min}$ for each month to be used in (21). A set of $(T_{\max}, T_{\min})$ values can be obtained from two sets of $(T_{\text{sat}}, T^*)$ via (21). Thus, given the four average $(T_{\text{sat}}, T^*)$ obtained for each month, six values for $(T_{\max}, T_{\min})$ were obtained for each month. These six were averaged and used to scale (23) to each month (using the same constants presented in Table I). The RMS deviation of the result at each satellite overpass time from the average satellite measurements was 3.6 K when computed over all months. This is reasonable given that the overall uncertainty in the satellite measurements is estimated not to exceed 1.6 K. Future work on obtaining $T_s$ in between MODIS overpasses may involve developing a reduced order model of that presented herein, or perhaps including a full version of that model combined with an atmospheric model as well.

To compare the value of $u_{10}$ used in the simulations with the ASOS measurements, the correlation coefficient between the two was computed. Specifically, $u_{10}$ used in the simulations was compared to those measured at three neighboring weather

TABLE IV
TOP ROW: CORRELATION COEFFICIENT, $R$, BETWEEN MEASURED $u_{10}$ AT INDIVIDUAL AIRPORTS (AND THEIR AVERAGE) WITH THE VALUE OF $u_{10}$ USED IN THE SIMULATIONS

| Wind Source | AND | GMU | CEU | AVG |
|---|---|---|---|---|
| SIM | −0.0075 | 0.0323 | 0.0042 | 0.0160 |
| AND | – | 0.0322 | 0.0181 | 0.6357 |
| GMU | 0.0322 | – | 0.0035 | 0.5908 |
| CEU | 0.0181 | 0.0035 | – | 0.5330 |

Lower three rows: correlation coefficients of each airport with each other.

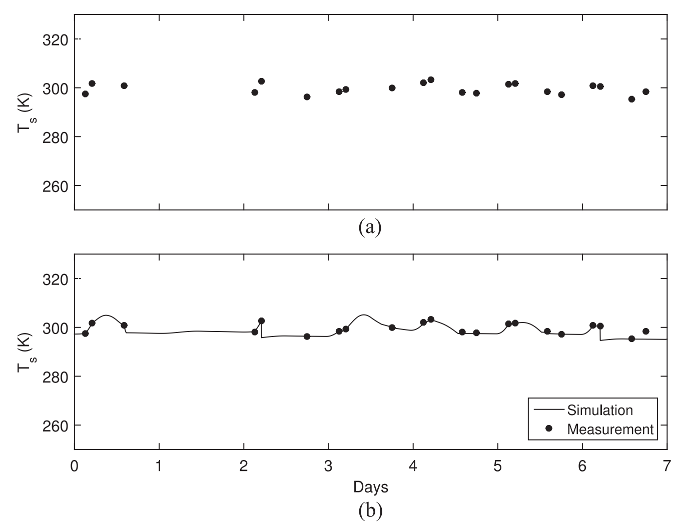


Fig. 24. Surface temperature, $T_s$, in K versus day from simulation results for a typical week where both $u_{10}$ and $C_k^f$ are large. (a) Satellite measurements only. (b) Satellite measurements and simulation results.

stations: the Anderson Regional Airport (AND), the Greenville Downtown Airport (GMU), and the Oconee County Regional Airport (CEU). Additionally, the correlation coefficient was calculated using the average of the three stations. For comparison, the correlation coefficients of the wind measurements between each of the three airports were also calculated. The correlation coefficients are presented in Table IV. None of the correlation coefficients between the airport $u_{10}$ and the $u_{10}$ used in the simulations exceeded 0.04. This is not unexpected since the $u_{10}$ used in the simulations was essentially a free parameter used to force convergence, thereby accounting for several uncertainties in the simulation approach. However, referring to Table IV, $R$ is less than 0.04 for each of the airports compared with each other. Hence, the variability of $u_{10}$ over space is significant and $R$ should not be expected to be large between the simulated value and the airport values, regardless of the simulation approach taken. We note in passing that $R$ for the comparison of each airport with the average of the three airports is large. This is expected since each individual station counts for 1/3 of the average in the calculation.

A recognized source of error in the simulation algorithm comes from how $u_{10}$ is handled when the simulations select large values for $u_{10}$. The maximum allowed $u_{10}$ of 20 m/s for the simulation was chosen based on the maximum ASOS

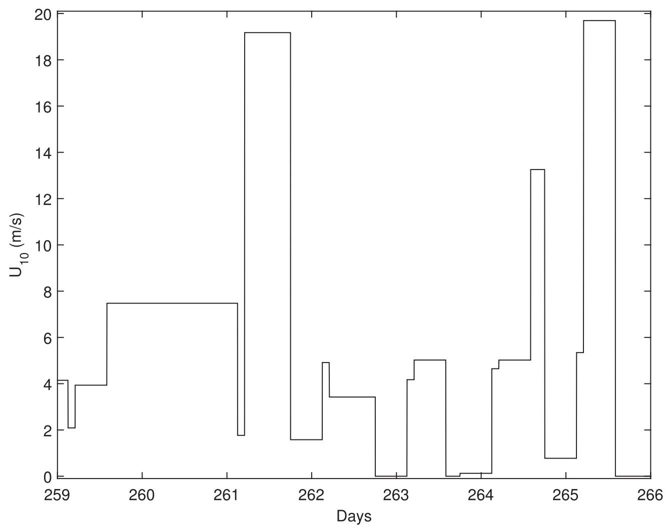


Fig. 25. Wind speed, $u_{10}$, in m/s versus day number from simulation results for a typical week.

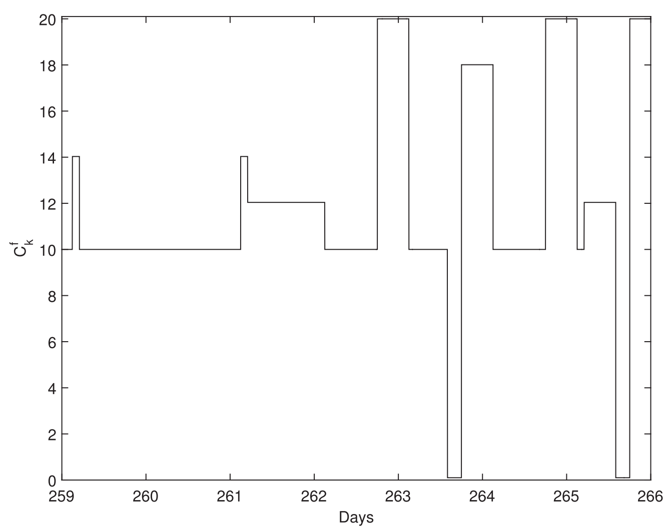


Fig. 26. Internal losses coefficient, $C_k^f$ versus day number from simulation results for a typical week.

measurement observed in the simulation time frame. However, due to the solving method, $u_{10}$ is set to 20 m/s more often than ASOS measurements predict, and setting $u_{10} = 20$ m/s generally results in large spikes in $T_s$. Simulation results for a sample week where $T_s$ experiences such a spike are shown in Fig. 24. The sharp change in temperature at day 6 occurs when both $u_{10}$ and $C_k^f$ are changing rapidly, as shown in the plots of $u_{10}$ versus time and $C_k^f$ versus time for that sample week in Figs. 25 and 26, respectively. This causes a rapid shift in $L$, shown for that sample week in Fig. 27, which causes the entrained water at $T_b$ to change $T_s$ rapidly. The first-order discontinuity in $T_s$ in this situation makes the simulation results less reliable. With more knowledge of $u_{10}$ on the lake surface, this error could be reduced, and this is left as future work. It is noted that these aforementioned errors occur during less than 7% of the simulation.

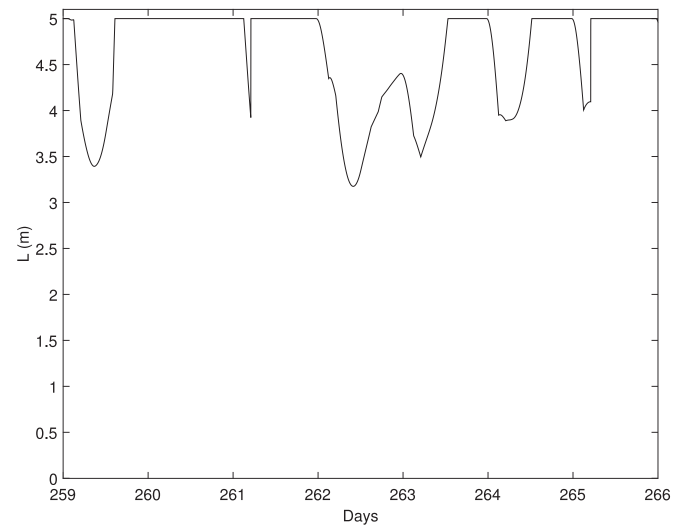


Fig. 27. Mixed layer depth, $L$, in m versus day number from simulation results for a typical week.

## VI. Conclusion

Simulations of lake surface temperature for Lake Hartwell were conducted using satellite surface temperature measurements as an input, along with ambient atmospheric conditions obtained from a nearby weather station. The simulation results were made dimensionless and were averaged to reveal the diurnal variation in $T_s$. The average diurnal trend is well approximated by a summation of the first four Fourier components. This functional form is an excellent approximation of the average annual trend and, to the authors' knowledge, is the first suggested functional form for $T_s$ on a lake surface.

## Acknowledgment

Surface temperature and cloud cover data were obtained from the MODIS Adaptive Processing System, part of the NASA Earth-Sun System Division. Ambient atmospheric measurement data were acquired from the National Oceanic and Atmospheric Administration (NOAA). The authors thank R. Phillips for providing processed versions of the satellite data and for his insights in support of this study.

## References

[1] D. T. Llewellyn-Jones, C. T. Mutlow, A. M. Zavody, M. J. Murray, M. R. Allen, R. W. Saunders, and I. J. Barton, "SST measurements from ATSR on ESAS ERS-1 satellite - early results," in *Proc. 13th Annu. Int. Geosci. Remote Sensing Symp.*, Aug. 1993, pp. 155–156.

[2] NASA, *Landsat 7 Science Data Users Handbook*. Washington, DC, USA: NASA, 2000.

[3] M. Sutterlin, C. B. Schaaf, R. Stockli, Q. Sun, R. Husler, and S. Neuhaus, C. Ad Wunderle, "Albedo and reflectance anisotropy retrieval from AVHRR operated onboard NOAA and MetOp satellites: Algorithm performance and accuracy assessment for Europe," *Remote Sensing Environment*, vol. 168, pp. 163–176, 2015.

[4] NASA, *NASA Land Processes Distributed Active Archive Center (LP DAAC): MOD06L2, MYD06L2, MOD11A1, and MYD11A1*. Washington, DC, USA: NASA/USGS, 2014.

[5] G. Liu, W. Ou, Y. Zhang, T. Wu, G. Zhu, K. Shi, and B. Qin, "Validating and mapping surface water temperatures in Lake Taihu: Results from MODIS land surface temperature products," *IEEE J. Sel. Topics Appl. Earth Observ. Remote Sens.*, vol. 8, no. 3, pp. 1230–1244, Mar. 2015.

[6] C. Strong, A. K. Kochanski, and E. T. Crosman, "A slab model of the Great Salt Lake for regional climate change," *J. Adv. Model. Earth Syst.*, vol. 6, pp. 602–615, 2014.

[7] J. A. Grim, J. C. Knievel, and E. T. Crosman, "Techniques for using MODIS data to remotely sense lake water surface temperatures," *J. Atmospheric Oceanic Technol.*, vol. 30, pp. 2434–2451, 2013.

[8] S. Sima, A. Ahmadalipour, and M. Tajrishy, "Mapping surface temperature of a hyper-saline lake and investigating the effect of temperature distribution on the lake evaporation," *Remote Sensing Environment*, vol. 136, pp. 374–385, 2013.

[9] F. Xiao, F. Ling, Y. Du, Q. Feng, Y. Yan, and H. Chen, "Evaluation of spatial-temporal dynamics in surface water temperature of Qinghai Lake from 2001 to 2010 by using MODIS data," *J. Arid Land*, vol. 5, pp. 452–464, 2013.

[10] Z.-L. Li, B.-H. Tang, H. Wu, H. Ren, G. Yan, Z. Wan, I. F. Trigo, and J. A. Sobrino, "Satellite-derived land surface temperature: Current status and perspectives," *Remote Sensing Environment*, vol. 131, pp. 14–37, 2013.

[11] E. T. Crosman and J. D. Horel, "MODIS-derived surface temperature of the Great Salt Lake," *Remote Sensing Environment*, vol. 113, pp. 73–81, 2009.

[12] A. Reinart and M. Reinhold, "Mapping surface temperature in large lakes with MODIS data," *Remote Sensing Environment*, vol. 112, pp. 603–611, 2008.

[13] D. C. Oesch, J.-M. Jaquet, A. Hauser, and S. Wunderle, "Lake surface water temperature retrieval using advanced very high resolution radiometer and Moderate Resolution Imaging Spectroradiometer data: Validation and feasibility study," *J. Geophys. Res. Atmospheres*, vol. 110, p. C12014, 2005.

[14] M. P. Curtarelli, E. Alcântara, C. D. Rennó, A. T. Assireu, M. P. Bonnet, and J. L. Stech, "Modelling the surface circulation and thermal structure of a tropical reservoir using three-dimensional hydrodynamic lake model and remote-sensing data," *J. Water Environ.*, vol. 28, pp. 516–525, 2014.

[15] B. Deng, S. Liu, W. Xiao, W. Wang, J. Jin, and X. Lee, "Evaluation of the CLM4 lake model at a large and shallow freshwater lake," *J. Hydrometeorology*, vol. 14, pp. 636–649, 2013.

[16] R. C. Wilson, S. J. Hook, P. Schneider, and S. G. Schladow, "Skin and bulk temperature difference at Lake Tahoe: A case study on lake skin effect," *J. Geophysical Res.*, vol. 118, pp. 10332–10346, 2013.

[17] H. Grassl, "The dependence of the measured cool skin of the ocean on wind stress and heat flux," vol. 10, pp. 465–475, 1976.

[18] E. D. McAlister and W. McLeish, "Heat transfer in the top millimeter of the ocean," *J. Geophysical Res.*, vol. 74, pp. 3408–3414, 1969.

[19] K. B. Katsaros, W. T. Liu, J. A. Businger, and J. E. Tillman, "Heat transport and thermal structure in the interfacial boundary layer measured in an open tank of water in turbulent free convection," *J. Fluid Mech.*, vol. 83, pp. 311–335, 1977.

[20] R. Phillips, J. R. Saylor, N. B. Kaye, and J. Gibert, "A comparison of remote sensing estimates of lake evaporation with pan evaporation measurements along the Savannah River Basin," presented at the South Carolina Water Resources Conf., Columbia, SC, USA, 2014.

[21] V. L. Nadolski, *Automated Surface Observing System (ASOS) User's Guide*, NOAA, DoD, FAA, U.S. Navy, 1998.

[22] W. Zhengming, "MODIS land-surface temperature algorithm theoretical basis document (LST ATBD)," Inst. Comput. Earth Syst. Sci., Univ. California, Santa Barbara, CA, USA, Tech. Rep., 1999.

[23] E. H. Alcântara, J. L. Stech, J. A. Lorenzzetti, M. P. Bonnet, X. Casamitjana, A. T. Assireu, and E. M. Novo, "Remote sensing of water surface temperature and heat flux over a tropical hydroelectric reservoir," *Remote Sensing Environment*, vol. 114, pp. 2651–2665, 2010.

[24] B. Henderson-Sellers, "Calculating the surface energy balance for lake and reservoir modeling: A review," *Rev. Geophys.*, vol. 24, pp. 625–649, 1986.

[25] I. Reda and A. Andreas, "Solar position algorithm for solar radiation applications," Nat. Renewable Energy Lab., Golden, CO, USA, Tech. Rep. 560-34302, 2008.

[26] R. K. Reed, "On estimating insolation over the ocean," *J. Phys. Oceanography*, vol. 7, pp. 482–485, 1977.

[27] I. Y. Fung, "On the variability of the net longwave radiation at the ocean surface," *Rev. Geophysics Space Phys.*, vol. 22, pp. 177–193, 1984.

[28] P. R. Lowe, "An approximating polynomial for the computation of saturation vapor pressure," *J. Appl. Meteorology*, vol. 16, pp. 100–103, 1976.

[29] W. G. Large, "Sensitivity to surface forcing and boundary layer mixing in a global ocean model: Annual-mean climatology," *J. Phys. Oceanography*, vol. 27, pp. 2418–2447, 1997.

[30] W. M. Lewis Jr, "A revised classification of lakes based on mixing," *Can. J. Fish Aquatic Sci.*, vol. 40, pp. 1779–1787, 1983.

[31] H. B. Fischer, E. J. List, R. C. Y. Koh, J. Imberger, and N. H. Brooks, *Mixing in Inland and Coastal Waters*. London, U.K.: Academic, 1979.

[32] J. Imberger, "The diurnal mixed layer," *Limnology Oceanography*, vol. 30, pp. 737–770, 1985.

[33] S. Seker-Elci, "Modeling of hydrodynamic circulation and cohesive sediment transport and prediction of shoreline erosion in Hartwell Lake, SC/GA," Ph.D. dissertation, Georgia Inst. of Technol., Atlanta, GA, USA, 2004.

[34] D. M. Snider and R. Viskanta, "Combined conduction-radiation energy transfer in stagnant water," *Water Resources Res.*, vol. 10, pp. 939–946, 1974.

[35] S. S. Girgis and A. C. Smith, "On thermal stratification in stagnant lakes," *Int. J. Eng. Sci.*, vol. 18, pp. 69–79, 1980.

[36] P. P. Niiler and E. B. Kraus, "One-dimensional models of the upper ocean," in *Modelling and Prediction of the Upper Layers of the Ocean*. New York, NY, USA: Pergamon Press, 1977, pp. 143–172.

[37] R. H. Spigel, J. Imberger, and K. N. Rayner, "Modelling the diurnal mixed layer," *Limnology Oceanography*, vol. 31, pp. 533–556, 1986.

[38] E. T. Crosman and J. D. Horel, "Sea and lake breezes: A review of numerical studies," *Boundary-Layer Meteorol.*, vol. 137, pp. 1–29, 2010.

[39] C. J. Willmott, S. M. Robeson, and K. Matsuura, "A refined index of model performance," *Int. J. Climatology*, vol. 32, pp. 2088–2094, 2012.

[40] C. Coll, Z. Wan, and J. M. Galve, "Temperature-based and radiance-based validations of the V5 MODIS land surface temperature product," *J. Geophysical Res.*, vol. 114, p. D20102, 2009.

[41] K. Schneider and W. Mauser, "Processing and accuracy of Landsat Thematic Mapper data for lake surface temperature measurement," *Int. J. Remote Sensing*, vol. 17, pp. 2027–2041, 1996.

[42] P. Schneider and S. J. Hook, "Space observations of inland water bodies show rapid surface warming since 1985," *Geophysical Res. Lett.*, vol. 37, 2010, Art. no. L22405.

[43] M. Jin and R. E. Dickinson, "Interpolation of surface radiative temperature measured from polar orbiting satellites to a diurnal cycle," *J. Geophysical Res.*, vol. 104, pp. 2105–2116, 1999.


**Jonathan L. Hodges** received the B.S. and M.S. degrees in mechanical engineering from Clemson University, Clemson, SC, USA. He is currently working toward the Ph.D. degree at Virginia Polytechnic Institute and State University, Blacksburg, VA, USA.

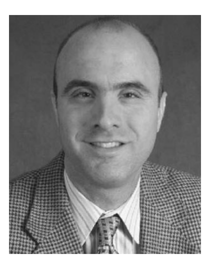

**John R. Saylor** received the B.S. degree from the State University of New York at Buffalo, Buffalo, NY, USA, the M.S. degree from the University of Minnesota, Minneapolis, MN, USA, and the M.Phil. and Ph.D. degrees from Yale University, New Haven, CT, USA, all in mechanical engineering.

He is currently a Professor of mechanical engineering at Clemson University, Clemson, SC, USA.

**Nigel B. Kaye** received the B.E. degree from the University of New South Wales, Sydney, NSW, Australia, and the Ph.D. degree from the University of Cambridge, Cambridge, U.K.

He is currently an Associate Professor of civil engineering at Clemson University, Clemson, SC, USA.